Letter

Transport-generated signals uncover geometric features of evolving branched structures

Fabian H. Kreten, Ludger Santen, and Reza Shaebani*
Department of Theoretical Physics and Center for Biophysics, Saarland University, 66123 Saarbrücken, Germany

(Received 13 June 2025; revised 12 November 2025; accepted 28 January 2026; published 3 March 2026)

Branched structures that evolve over time critically shape the function of diverse natural and engineered systems, from neuronal dendrites and vascular networks to pulmonary and root architectures. Inferring their hidden geometric properties and monitoring their morphological evolution remain major challenges, as direct imaging or tracer tracking is often infeasible, especially in living systems. Here, we introduce a general theoretical framework to recover the structural features of evolving branched geometries by analyzing the collective signals generated by tracer particles during transport. As tracers traverse the structure, they emit detectable pulses upon reaching an observation site. We show that the statistical properties of the resulting signal intensity, which reflects underlying first-passage dynamics, encode key morphological descriptors such as network extent, directional bias, and local trapping frequency. The strength of our approach lies in enabling quantitative inference of geometric parameters from time-series data recorded at a single observation site. This theoretical framework is designed to guide and motivate future experimental studies in systems where direct imaging is not feasible. Unlike conventional tracer-tracking methods, our approach enables noninvasive inference of hidden geometry solely from externally measurable signals, requiring no access to individual trajectories or internal measurements. This conceptual advance opens an avenue for transport-based structural inference and provides a scalable strategy for probing dynamic, complex architectures across biological, physical, and synthetic systems.

DOI: 10.1103/bnnl-xnm6

Dynamic branched structures govern the transport of matter, energy, and information across diverse systems, from river basins and pulmonary and root architectures to neuronal dendrites, synthetic porous materials, and power or communication networks, and even to abstract frameworks such as epidemic or search networks [1–22]. Recovering the geometric properties and monitoring the structural evolution of such complex architectures remain major challenges, as their internal structures are often hidden, transient, or inaccessible to direct imaging and tracer tracking, particularly in living systems. Yet, structure critically determines function in many biological contexts. For example, quantifying the degeneration of neuronal dendrites can crucially help to monitor the progression of neurodegenerative diseases such as Alzheimer's [21,23].

Diffusive tracers have long been used to probe labyrinthine environments by connecting transport statistics to geometry [22,24–32]. However, conventional tracer-tracking approaches demand direct high-resolution observation of individual trajectories and often involve invasive measurements or incomplete statistics within the timescales of structural evolution. To overcome these substantial technical challenges (particularly in biological systems), we propose an alternative paradigm: Tracers emit externally detectable signals only upon reaching a designated observation site, generating a collective, time-resolved signal intensity. We show that this aggregated signal retains the statistical imprint of the underlying geometry, enabling indirect and noninvasive inference of structural properties from externally measurable data.

We develop a general predictive framework that quantitatively links the temporal statistics of signals generated by tracers at a fixed (arbitrarily chosen) detection point to hidden geometric features of evolving branched structures (see Fig. 1). The analysis establishes an explicit, invertible mapping between measurable signal characteristics and structural parameters such as network extent, directional bias (e.g., due to tapering toward or away from the leaves), and local trapping frequency (arising from boundary stickiness, internal traps, or transient caging at junctions and branch segments). Importantly, the approach requires no trajectory reconstruction or access to all internal nodes, making it suitable for noninvasive probing of living or otherwise inaccessible systems. To demonstrate feasibility and practical relevance, we apply the framework to neuronal dendrites and outline in the Supplemental Material [33] additional potential applications, including pulmonary, vascular, and plant root architectures. We further perform numerical validation using synthetic signals, confirming the accuracy of parameter recovery and the robustness of the framework. Although the qualitative trends linking signal features to geometry are expected from known first-passage properties, the central advance here is the ability to extract quantitative structural parameters from single-point time-series measurements, thereby providing concrete predictions for future experimental validation. Together, these

*Contact author: shaebani@lusi.uni-sb.de

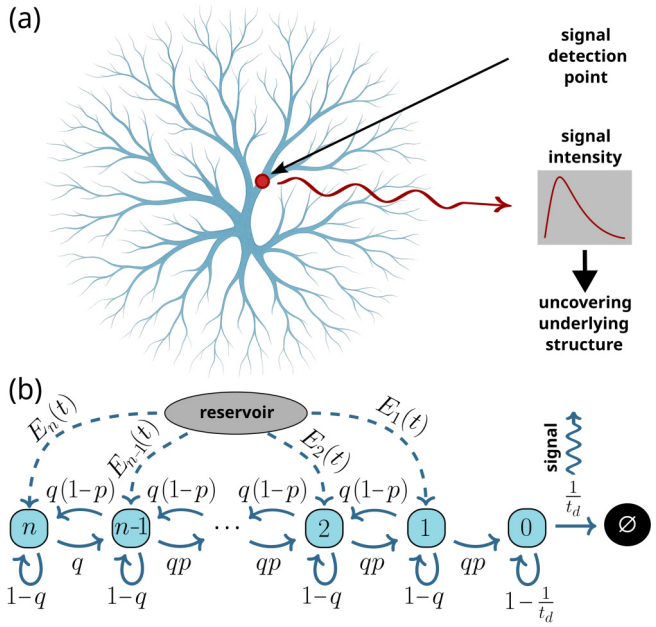

FIG. 1. (a) Schematic illustration of a branched structure with a fixed detection point that registers tracer-generated signals used for structural inference. (b) Illustrative example of transitions and boundary conditions in the model.

developments establish a versatile and experimentally viable route for noninvasive structural inference in evolving branched systems.

Branched structure model. We adopt a coarse-grained perspective and consider a branched tree structure consisting of n generations of nodes with mean internode spacing L (total extent nL). Noninteracting tracer particles perform stochastic hopping between the nodes of the tree [5]. Initially, a reservoir contains $\mathcal{N}$ tracers that can enter the tree at random nodes and times [see Fig. 1(b)]. The framework accommodates arbitrary entry and boundary conditions as well as system-specific structural and dynamical details. We consider an example in the following, where the joint entry distribution combines an exponential entry-position probability, representing spatially homogeneous introduction of tracers over the accessible surface or volume of the tree, and a geometric entry-time distribution with mean t_e. For a binary tree, the combined entry distribution at depth $i \in [0, n]$ ($i = 0$ denoting the main root and $i = n$ the leaves) and time t is $E_i(t) = \frac{1}{t_e}(1 - \frac{1}{t_e})^t \frac{2^{i-1}}{2^n - 1}$. This choice is motivated by the fact that the geometric distribution has maximal entropy among all distributions with a given mean; i.e., it does not implicitly add further assumptions. For illustrative purposes, it is therefore sufficient as a placeholder for more complex scenarios such as the inference of structural properties or the monitoring of structural evolution across a large ensemble of units (e.g., neuronal dendrites within a brain region) each with a random delay of entry. A similar argument applies to the choice of the signal emission time distribution discussed below. In practice, the entry-time distribution is determined by the experimental protocol and the specific system under study. Alternative configurations, such as single-point injection relevant for pulmonary or vascular structures, can be readily incorporated by modifying the injection term (see the Supplemental Material [33]).

At each observation time step Δt, a tracer either spontaneously hops to a neighboring node with probability q or remains at its current node with probability $1 - q$, leading to a geometrically distributed waiting time at each node. The mean escape time from a node to any neighboring furcation in real time is $\langle t \rangle = \Delta t / q$, which captures stochastic trapping due to sticky or roughened boundaries, transient caging along the structure, or travel time between bifurcations. In systems with sticky boundaries, $\langle t \rangle \propto \omega_m/(\omega_m + \omega_w)$, where ω_m and ω_w denote unbinding and binding rates; in geometrically caged environments, $\langle t \rangle \propto 1 + \frac{V_{\text{cages}}}{V_{\text{channel}}}$, where V_{cages} and V_{channel} are the volume of localized traps and accessible transport channels (see the Supplemental Material [33] and Ref. [34]). Thus, q physically reflects microscopic escape dynamics, and the mapping through $\langle t \rangle$ ensures consistent timescales between the coarse-grained model and the underlying physical process.

A topological bias parameter p accounts for directional preference in tracer motion. At each step, a tracer hops toward the root with probability p, or toward the leaves with probability $1 - p$. This bias can stem from imposed flows or geometrical asymmetries such as tapering of branch cross sections. For purely diffusive transport on symmetric trees composed of cylindrical branches with furcation number $\mathfrak{z}$ and neglecting complications at the branch points, the directional bias can be estimated as $p = \frac{A_p}{A_p + (\mathfrak{z}-1)A_c}$. The cross-sectional areas A_p and A_c of parent and child branches are related by the allometric scaling $d_p^\kappa = \sum_{i=1}^{\mathfrak{z}-1} d_c^\kappa$, where d_p and d_c are the diameters of parent and child branches at a furcation, and κ is an allometric exponent. Typical empirical exponents are $\kappa = \frac{3}{2}$ for neuronal dendrites, $\kappa = 2$ for botanical trees, and $\kappa = 3$ for vascular or pulmonary networks [4,8,35,36]. Assuming bifurcations ($\mathfrak{z} = 3$) and symmetric daughter branches yields representative values of $p \simeq 0.56$, 0.5, and 0.44, respectively, in these cases. For general channel profiles and driving forces, p can be determined by solving a Fick-Jacobs-like equation, which provides a physically interpretable and experimentally tunable link between geometry, flow, and directional bias (see the Supplemental Material [33] for details).

As a proof of concept, we focus here on regular trees with uniform parameters n, q, p. However, the conclusions remain valid under moderate and realistic levels of structural irregularity. This robustness arises because the signal characteristics analyzed here are governed by first-passage dynamics—quantities that we have previously shown to be resilient to structural heterogeneity, for example, in the context of transport on neuronal dendrites [5,28].

Signal generation. Upon reaching the designated detection point, each tracer emits a transient pulse after a random delay, referred to as the *emission time*, drawn from a geometric distribution with mean t_d. The choice of the geometric distribution is again motivated by the maximal entropy argument and is therefore a sufficient placeholder for accounting for local activation processes (e.g., biochemical or electrical) required for signal generation. We point out that, due to the large number of tracers, the present case of a single pulse emitted after a geometrically distributed time is completely equivalent to the case of a geometrically decaying

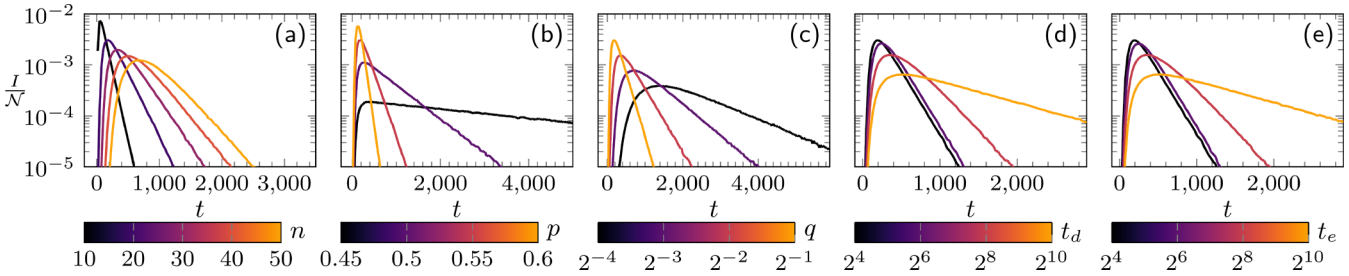

FIG. 2. Time evolution of the normalized signal intensity, averaged over bins of 30 time steps width, for varying model parameters. Reference values are $n=20$, $p=0.55$, $q=0.5$, and $t_e=t_d=1$. Each panel compares $I(t)$ for different values of (a) n, (b) p, (c) q, (d) t_d, and (e) t_e; the specific values used are listed in the color boxes.

signal with the same mean that is emitted upon reaching the detection point. In more general cases, when the emission times are distributed according to $\mathcal{D}(t)$, the signal is given by the convolution $I(t)=\sum_{\tau=0}^{t} f(\tau)\mathcal{D}(t-\tau)$, where $f(t)$ is the first-passage time distribution for traversing the structure, including the entry time. In turn, $f(t)$ can also be expressed as a convolution $f(t)=\sum_{\tau=0}^{t}\sum_{i=0}^{N} E_i(\tau)f_i(t-\tau)$, where $f_i(t)$ is the first-passage time distribution starting from node i and $E_i(t)$ is the general joint entry distribution for entering the network at node i at time t. The resulting pulses sum to the total measurable signal $I(t)$, from which the model parameters (n, p, q) are inferred. $I(t)$ thus reflects the combined statistics of three stochastic processes: entry, first passage, and emission. In the limit $t_e=t_d=1$, $I(t)$ reduces (up to scaling and time shift) to the first-passage time distribution. Analytical relations between (n, p, q) and first-passage quantities are provided elsewhere (see also Refs. [5,28]); however, as first-passage quantities are experimentally inaccessible, our framework instead infers the geometric features from the externally measurable signal $I(t)$.

The tracer injection and emission protocols used here are illustrative and can be adapted to system-specific constraints. The detection point can, in principle, be placed anywhere, though central locations are expected to yield more informative signals. The geometry and boundary conditions may also vary with the application. For clarity, we select the tree root as the detection point, mapping the transport problem onto an effective one-dimensional (1D) lattice—an approach common in analyses of finite Cayley trees and infinite Bethe lattices [28,37–41]. In this setting, the measurable signal follows $I(t+1)=P_0(t)/t_d$, where $P_0(t)$ is the occupation probability of the root at time t, directly linking the observed signal to transport dynamics. Figure 1(b) depicts the corresponding effective 1D lattice representation, with solid arrows indicating intersite transition probabilities and dashed arrows showing the total probability influx from external sources. The full dynamics are described by coupled master equations detailed in the Supplemental Material [33]. Together, these elements define a general predictive framework that links transport-generated time-series signals to structural properties of the underlying system via an explicit stochastic model. While we present the formulation for treelike geometries, the same modeling strategy can be adapted to other network architectures, entry protocols, and boundary conditions, with the choice of signal observables and inferred structural features tailored to the system of interest.

Signal processing. To evaluate whether the signal $I(t)$ contains sufficient information to recover the model parameters, we performed extensive Monte Carlo simulations with $\mathcal{N}=10^6$ tracer particles. Representative temporal profiles of $I(t)$ in Fig. 2 exhibit a pronounced peak followed by an exponential tail. The peak position, height, and decay rate vary systematically with the model parameters: The signal broadens and decays more slowly, showing a delayed lower maximum for increasing tree depth n, decreasing bias p or hopping probability q, or longer injection and emission delays t_e and t_d. $I(t)$ is invariant under exchange of t_e and t_d; the longer of the two timescales controls the asymptotic decay of $I(t)$.

To quantify how the signal depends on the structural parameters, we analyzed several shape descriptors of $I(t)$. When the entry and emission timescales (t_e and t_d) are moderate (i.e., short compared to the mean first-passage time through the structure), the observables group into two distinct behavioral classes in (n, p, q) space. For large t_e or t_d, this distinction fades and parameter identifiability decreases. Figure 3(a) shows the logarithm of the signal median, $m=\log_{10}(Q_{1/2})$, across (p, q) and (p, n) sections for representative t_e and t_d values (see also Fig. S8 of the Supplemental Material [33]). The median varies smoothly and monotonically with the model parameters; increasing t_e or t_d shifts it to later times without altering the overall landscape. Similar trends hold for the signal mean, higher moments, and peak height (not shown). A representative observable of the second class is the quartile coefficient of dispersion, $\mathrm{qcd}=\frac{Q_{3/4}-Q_{1/4}}{Q_{3/4}+Q_{1/4}}$, which quantifies the temporal dispersion of $I(t)$ ($Q_{i/4}$ denotes the ith quartile). At low t_e and t_d, qcd also varies smoothly and monotonically, but for larger timescales, nonmonotonic patterns and near-degeneracies emerge, where m and qcd become nearly colinear. Other observables in this class (e.g., normalized variance, skewness, and kurtosis) show similar behavior. The existence of only two independent classes of shape parameters implies that signal measurements constrain the system to a one-dimensional manifold in (n, p, q) space. Knowing one parameter (or a relation among them) then allows the others to be inferred uniquely.

To assess the influence of t_e and t_d and identify locally invertible regions of the mapping $\boldsymbol{\psi}$ from model to signal shape parameters, we simulated $I(t)$ over a regular grid in parameter space and extracted m and qcd. Figure 3(b) shows the resulting map for a representative (p, q) section. At small t_e and t_d, the

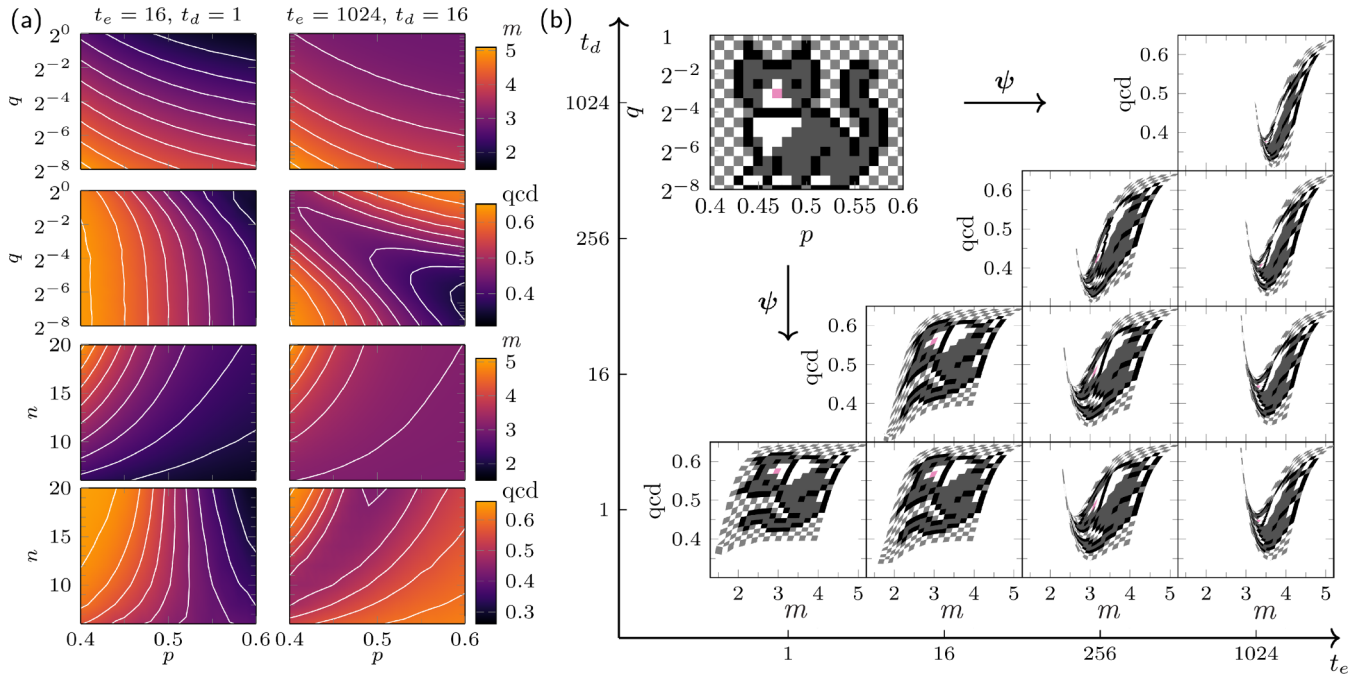

FIG. 3. (a) Heatmaps of m and qcd in the (p, q) section (upper panels, $n = 10$) and (p, n) section (lower panels, $q = 0.5$) of the model parameter space, shown for low (left column) and high (right column) values of t_e and t_d. (b) Effect of t_e and t_d on the mapping $\boldsymbol{\psi}$ from model parameters (p, q) to signal shape parameters (m, qcd), with $n = 10$. The local neighborhood of each sampled model parameter set is color-coded (inset), and their corresponding images in the signal parameter domain are colored with the same color (small panels). Due to symmetry under swapping $t_e \leftrightarrow t_d$, only cases with $t_e \geqslant t_d$ are shown.

mapping is nearly one-to-one and preserves structure under smooth deformations (e.g., flips or rotations). With increasing t_e and t_d, however, parts of the model space—particularly at high q—collapse into narrow bands in the signal parameter domain, signaling the breakdown of parameter extractability (see the Supplemental Material [33] for a detailed error analysis and numerical validation). Similar trends appear in other slices of (n, p, q) space (Fig. S9 of the Supplemental Material [33]).

Invertibility and experimental bounds. As demonstrated above, the signal $I(t)$ encodes structural information about the tree. Under moderate injection and emission timescales, two of the three core model parameters (n, p, q) can be reliably inferred from the shape characteristics of the signal. Recovering all three parameters uniquely, however, requires an additional independent observable, either a higher-order shape parameter or a complementary statistical measure. Approaches such as maximum-likelihood estimation, Kullback-Leibler divergence minimization, or empirical characteristic-function analysis could be employed for this purpose. The injection and detection timescales t_e and t_d may likewise be treated as estimable parameters. Overall, this framework establishes a foundation for noninvasive structural inference in branched systems, including delicate biological architectures such as neuronal dendrites.

A key limitation arises from the loss of invertibility in the high-q regime when either t_e or t_d become large. This reflects a fundamental constraint: The timescales of signal generation must remain compatible with those of the underlying transport dynamics. To quantify this condition, we identify a critical threshold q^* beyond which signal-based inference fails. Based on simulated data and a minimum-distance criterion in the (m, qcd) domain, we find $q^* \simeq \sqrt{\Delta t / \max(t_e, t_d)}$. Full resolution of the model across the entire (n, p, q) space requires that this threshold exceed the trap-free diffusion limit, $q = \Delta t \frac{2D}{L^2}$. This yields an upper bound on the temporal resolution,

$$\Delta t \leqslant \frac{L^4}{4D^2 \max(t_e, t_d)},$$

ensuring that invertibility is preserved. According to this equation, the range of invertibility is largest for $t_e = t_d = 1$, i.e., when t_d and t_e are minimal and the travel time between adjacent nodes exceeds the characteristic injection and emission timescales. When $t_e \propto 1/D_e$, with D_e denoting the diffusion constant in the exterior space, D_e enters the above equation and may constrain the feasibility of the approach by limiting the maximal allowable time resolution Δt.

Illustrative application: Neuronal dendrites. To illustrate the use of our framework in a concrete setting, we consider neuronal dendrites. (More applications are proposed in the Supplemental Material [33], including pulmonary airways, vascular networks, and plant root systems.) The complex and dynamic morphology of neuronal dendrites, including their elaborate branching patterns [Fig. 4(a)] and diverse spine geometries, enables the nervous system to form a network of signaling pathways and adjust function [42,43]. Neurodegenerative disorders such as Alzheimer's disease induce alterations in dendritic morphology, including changes in spine size, shape, and density, shaft thickness, and overall arbor extent [44,45]. While diagnosis and treatment of such diseases can crucially benefit from monitoring the morphological evolution of dendrites, direct noninvasive imaging or

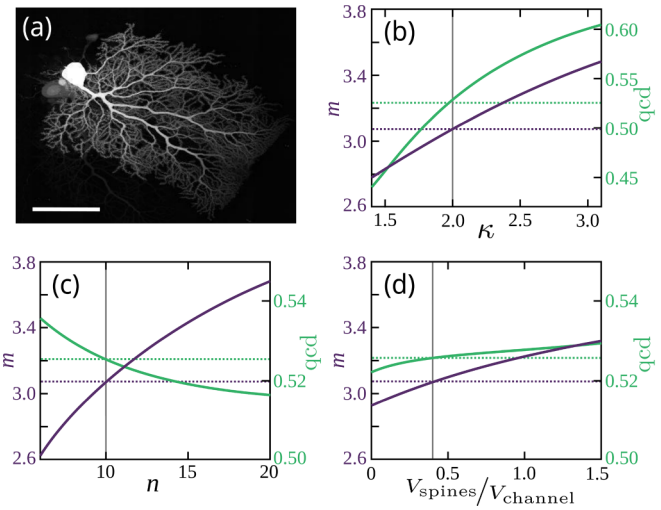

FIG. 4. (a) Dendritic branching structure of a cerebellar Purkinje neuron, adapted from Ref. [46]. Scale bar: 50 μm. Dependence of the signal parameters m and qcd on key dendritic structural quantities: the allometric exponent κ [panel (b)], tree depth n [panel (c)], and relative spine-to-shaft volume ratio [panel (d)], for $t_e = 1$ and $t_d = 16$. Vertical and horizontal lines mark the characteristic structural and corresponding signal parameter values of a typical healthy neuron [4,47–49].

tracer tracking over a large population of neurons within a reasonable time remains experimentally unfeasible. However, combining existing noninvasive techniques for real-time tracking of brain activity [50–52] with recent advances in brain-targeted drug delivery using lipid nanoparticles [53–55] opens the possibility of extracting structural information from externally measurable signals. A feasible implementation could involve engineered mRNA-carrying multilamellar liposomes that, upon targeted delivery to the brain, enter dendrites and diffusively traverse their complex arborization. When they reach the soma, mRNA molecules are released that encode a specific protein upon encountering ribosomes. The concentration of this protein over large neuronal populations could be externally measured (e.g., by magnetic resonance imaging) as a transient signal analogous to $I(t)$ in our model. Our signal generation proposal can stimulate further developments at the interface of neuroscience, molecular engineering, and pharmacology.

For quantitative validation, we generated synthetic signals using geometric entry and emission time distributions and varied dendritic structural parameters affected by disease: the number of junction generations n, the allometric exponent κ (related to the directional bias p toward the soma via $\kappa = \frac{-2\ln 2}{\ln(\frac{1-p}{2p})}$, and the relative spine-to-shaft volume ratio $\frac{V_{\mathrm{spines}}}{V_{\mathrm{channel}}} = \Delta t \frac{2D}{L^2 q} - 1$ [5]. Figure 4 presents the resulting dependencies of the signal statistical parameters m and qcd (generated by tracers at the soma) on these structural quantities across their biologically relevant ranges, with the healthy dendritic configuration indicated for reference [4,47–49]. Using a temporal resolution of $\Delta t \simeq 0.55$ s, consistent with typical dendritic branch lengths $L \simeq 10$ μm and diffusion times of green fluorescent protein in dendrites [56,57], we find that distinct morphological changes produce clearly separable variations in the signal characteristics. These results show that the evolving dendritic structure can be uniquely identified from measurable signal statistics.

We have developed a general and experimentally viable framework for inferring the hidden geometric features of evolving branched structures from externally measurable, transport-generated signals. Our approach establishes an explicit, parameter-invertible link between the collective signal statistics and key structural characteristics, such as network extent, directional bias, and localized trapping, without requiring direct tracer tracking. This conceptual advance opens an avenue for noninvasive structural inference across biological, physical, and synthetic systems. As demonstrated for neuronal dendrites and further examples in the Supplemental Material file [33] (pulmonary, vascular, and plant root networks), the proposed strategy provides a realistic route not only for probing evolving architectures but also for quantitatively identifying structural parameters and monitoring their evolution, provided that the scale of structural change exceeds the measurement uncertainty imposed by the signal statistics. While we do not present direct experimental data here, the framework yields quantitative, testable predictions that can directly inform and stimulate future experimental investigations. In this sense, the method goes beyond identifying qualitative trends and establishes a practical route for extracting geometric information from minimal, externally accessible measurements. Beyond treelike geometries, the framework can be extended to networks with loops, irregular topologies, or active transport mechanisms. Future directions include accounting for noisy or incomplete measurements, populations with structural diversity, exploring interacting tracer dynamics, and integrating statistical inference in combination with machine-learning tools to enhance precision and scalability. These developments position the method as a versatile foundation for next-generation noninvasive structural characterization in complex systems. As a concrete example, the feasibility of noninvasively detecting transport-generated signals from neuronal dendrites even when their detailed geometry is inaccessible to imaging has been recently demonstrated and discussed in detail in Ref. [58].

Acknowledgments. This work was supported by the Deutsche Forschungsgemeinschaft (DFG) within the collaborative research center SFB 1027 and also via grants INST 256/539-1, which funded the computing resources at Saarland University. R.S. acknowledges support by the Young Investigator Grant of Saarland University, Grant No. 7410110401. ChatGPT (OpenAI) was used to enhance readability. The authors take full responsibility for the content.

Data availability. The data that support the findings of this article are openly available [59].

[1] P. Ball, *Branches: Nature's Patterns: A Tapestry in Three Parts* (Oxford University Press, Oxford, UK, 2009).

[2] L. Koçillari, *et al.*, The widened pipe model of plant hydraulic evolution, Proc. Natl. Acad. Sci. USA **118**, e2100314118 (2021).

[3] S. Randriamanantsoa, A. Papargyriou, H. C. Maurer, K. Peschke, M. Schuster, G. Zecchin, K. Steiger, R. Öllinger, D. Saur, C. Scheel, R. Rad, E. Hannezo, M. Reichert, and A. R. Bausch, Spatiotemporal dynamics of self-organized branching in pancreas-derived organoids, Nat. Commun. **13**, 5219 (2022).

[4] M. Liao, X. Liang, and J. Howard, The narrowing of dendrite branches across nodes follows a well-defined scaling law, Proc. Natl. Acad. Sci. USA **118**, e2022395118 (2021).

[5] R. Jose, L. Santen, and M. R. Shaebani, Trapping in and escape from branched structures of neuronal dendrites, Biophys. J. **115**, 2014 (2018).

[6] J. T. Perron, P. W. Richardson, K. L. Ferrier, and M. Lapôtre, The root of branching river networks, Nature (London) **492**, 100 (2012).

[7] P. Desai-Chowdhry, A. B. Brummer, and V. M. Savage, How axon and dendrite branching are guided by time, energy, and spatial constraints, Sci. Rep. **12**, 20810 (2022).

[8] S. V. Grigoriev, O. D. Shnyrkov, P. M. Pustovoit, E. G. Iashina, and K. A. Pshenichnyi, Experimental evidence for logarithmic fractal structure of botanical trees, Phys. Rev. E **105**, 044412 (2022).

[9] A. Rinaldo, R. Rigon, J. R. Banavar, A. Maritan, and I. Rodriguez-Iturbe, Evolution and selection of river networks: Statics, dynamics, and complexity, Proc. Natl. Acad. Sci. USA **111**, 2417 (2014).

[10] D. Borse and B. Biswal, A novel probabilistic model to explain drainage network evolution, Adv. Water Resour. **171**, 104342 (2023).

[11] B. Wu, Y. Lin, Z. Zhang, and G. Chen, Trapping in dendrimers and regular hyperbranched polymers, J. Chem. Phys. **137**, 044903 (2012).

[12] B. Zhou, Q. Cheng, Z. Chen, Z. Chen, D. Liang, E. A. Munro, G. Yun, Y. Kawai, J. Chen, T. Bhowmick, K. K. Padmanathan, L. G. Occhipinti, H. Matsumoto, J. W. Gardner, B.-L. Su, and T. Hasan, Universal Murray's law for optimised fluid transport in synthetic structures, Nat. Commun. **15**, 3652 (2024).

[13] X. Zheng, G. Shen, C. Wang, Y. Li, D. Dunphy, T. Hasan, C. J. Brinker, and B.-L. Su, Bio-inspired Murray materials for mass transfer and activity, Nat. Commun. **8**, 14921 (2017).

[14] J. R. Banavar, A. Maritan, and A. Rinaldo, Size and form in efficient transportation networks, Nature (London) **399**, 130 (1999).

[15] B. Schäfer, T. Pesch, D. Manik, J. Gollenstede, G. Lin, H.-P. Beck, D. Witthaut, and M. Timme, Understanding Braess' paradox in power grids, Nat. Commun. **13**, 5396 (2022).

[16] L. Yang, H. Xiao, Y. Qian, X. Zhao, X.-Y. Kong, P. Liu, W. Xin, L. Fu, L. Jiang, and L. Wen, Bioinspired hierarchical porous membrane for efficient uranium extraction from seawater, Nat. Sustain. **5**, 71 (2022).

[17] R. Pastor-Satorras, C. Castellano, P. V. Mieghem, and A. Vespignani, Epidemic processes in complex networks, Rev. Mod. Phys. **87**, 925 (2015).

[18] M. E. J. Newman, *Networks: An Introduction* (Oxford University Press, New York, 2010).

[19] J. M. Kleinberg, Navigation in a small world, Nature (London) **406**, 845 (2000).

[20] B. Bollobás and O. Riordan, Shortest paths and load scaling in scale-free trees, Phys. Rev. E **69**, 036114 (2004).

[21] N. Spruston, Pyramidal neurons: dendritic structure and synaptic integration, Nat. Rev. Neurosci. **9**, 206 (2008).

[22] M. Felici, M. Filoche, and B. Sapoval, Renormalized random walk study of oxygen absorption in the human lung, Phys. Rev. Lett. **92**, 068101 (2004).

[23] M. P. Forrest, E. Parnell, and P. Penzes, Dendritic structural plasticity and neuropsychiatric disease, Nat. Rev. Neurosci. **19**, 215 (2018).

[24] D. ben Avraham and S. Havlin, *Diffusion and Reactions in Fractals and Disordered Systems* (Cambridge University Press, Cambridge, UK, 2000).

[25] R. W. Mair, G. P. Wong, D. Hoffmann, M. D. Hürlimann, S. Patz, L. M. Schwartz, and R. L. Walsworth, Probing porous media with gas diffusion NMR, Phys. Rev. Lett. **83**, 3324 (1999).

[26] P. Tierno and M. R. Shaebani, Enhanced diffusion and anomalous transport of magnetic colloids driven above a two-state flashing potential, Soft Matter **12**, 3398 (2016).

[27] R. Krishna, Describing the diffusion of guest molecules inside porous structures, J. Phys. Chem. C **113**, 19756 (2009).

[28] M. R. Shaebani, R. Jose, C. Sand, and L. Santen, Unraveling the structure of treelike networks from first-passage times of lazy random walkers, Phys. Rev. E **98**, 042315 (2018).

[29] F. H. Kreten, L. Santen, and R. Shaebani, Inferring tree structure with hidden traps from first-passage times, Phys. Rev. E **112**, 054306 (2025).

[30] Y. Siantos, C. Cooper, and T. Radzik, Fast low-cost estimation of network properties using random walks, Internet Math. **12**, 221 (2016).

[31] E. Agliari, R. Burioni, D. Cassi, and F. M. Neri, Autocatalytic reaction on low-dimensional substrates, Theor. Chem. Acc. **118**, 855 (2007).

[32] Z. Sadjadi, M. Miri, M. R. Shaebani, and S. Nakhaee, Diffusive transport of light in a two-dimensional disordered packing of disks: Analytical approach to transport mean free path, Phys. Rev. E **78**, 031121 (2008).

[33] See Supplemental Material at http://link.aps.org/supplemental/10.1103/bnnl-xnm6 for (1) the analytical proofs of mapping between the model parameters and geometric characteristics of the structure, (2) an error analysis and numerical validation section, (3) three illustrative applications of our proposed approach, and (4) a few figures that illustrate the mapping between these two phase spaces, which also includes Refs. [60–75].

[34] L. Dagdug, A. M. Berezhkovskii, Y. A. Makhnovskii, and V. Y. Zitserman, Transient diffusion in a tube with dead ends, J. Chem. Phys. **127**, 224712 (2007).

[35] C. D. Murray, The physiological principle of minimum work: I. The vascular system and the cost of blood volume., Proc. Natl. Acad. Sci. USA **12**, 207 (1926).

[36] W. Rall, Branching dendritic trees and motoneuron membrane resistivity, Exp. Neurol. **1**, 491 (1959).

[37] E. Agliari, A. Blumen, and O. Mülken, Dynamics of continuous-time quantum walks in restricted geometries, J. Phys. A **41**, 445301 (2008).

[38] R. Metzler, S. Redner, and G. Oshanin, *First-Passage Phenomena and Their Applications* (World Scientific, Singapore, 2014), pp. 96–121.

[39] S. Redner, *A Guide to First-Passage Processes* (Cambridge University Press, Cambridge, UK, 2001).

[40] B. D. Hughes and M. Sahimi, Random walks on the Bethe lattice, J. Stat. Phys. **29**, 781 (1982).

[41] L. Skarpalezos, A. Kittas, P. Argyrakis, R. Cohen, and S. Havlin, Anomalous biased diffusion in networks, Phys. Rev. E **88**, 012817 (2013).
[42] Y.-N. Jan and L. Y. Jan, Branching out: Mechanisms of dendritic arborization, Nat. Rev. Neurosci. **11**, 316 (2010).
[43] H. Hering and M. Sheng, Dendritic spines: Structure, dynamics and regulation, Nat. Rev. Neurosci. **2**, 880 (2001).
[44] P. Penzes, M. E. Cahill, K. A. Jones, J.-E. VanLeeuwen, and K. M. Woolfrey, Dendritic spine pathology in neuropsychiatric disorders, Nat. Neurosci. **14**, 285 (2011).
[45] C. Tackenberg, A. Ghori, and R. Brandt, Thin, stubby or mushroom: Spine pathology in Alzheimer's disease, Curr. Alzheimer Res. **6**, 261 (2009).
[46] M. Martone, D. Price, A. Thor, H. Hakozaki, and M. Terada, CIL:40021, *Mus musculus*, Purkinje cell. Cil. Dataset (RRID:SCR_003510) (2012), https://doi.org/doi:10.7295/W9CIL40021.
[47] R. Benavides-Piccione, I. Fernaud-Espinosa, V. Robles, R. Yuste, and J. DeFelipe, Age-based comparison of human dendritic spine structure using complete three-dimensional reconstructions, Cereb. Cortex **23**, 1798 (2013).
[48] M. Rapp, I. Segev, and Y. Yarom, Physiology, morphology and detailed passive models of guinea-pig cerebellar Purkinje cells, J. Physiol. **474**, 101 (1994).
[49] K. M. Harris, F. E. Jensen, and B. Tsao, Three-dimensional structure of dendritic spines and synapses in rat hippocampus (CA1) at postnatal day 15 and adult ages: implications for the maturation of synaptic physiology and long-term potentiation, J. Neurosci. **12**, 2685 (1992).
[50] J. A. Stanley and N. Raz, Functional magnetic resonance spectroscopy: The new MRS for cognitive neuroscience and psychiatry research, Front. Psychiatry **9**, 76 (2018).
[51] S. D. Bass, S. Mariazzi, P. Moskal, and E. Stepien, *Colloquium*: Positronium physics and biomedical applications, Rev. Mod. Phys. **95**, 021002 (2023).
[52] R. S. Koolschijn, W. T. Clarke, I. B. Ip, U. E. Emir, and H. C. Barron, Event-related functional magnetic resonance spectroscopy, NeuroImage **276**, 120194 (2023).
[53] Z. Zhang, J. Guan, Z. Jiang, Y. Yang, J. Liu, W. Hua, Y. Mao, C. Li, W. Lu, J. Qian, and C. Zhan, Brain-targeted drug delivery by manipulating protein corona functions, Nat. Commun. **10**, 3561 (2019).
[54] C. Saraiva, C. Praca, R. Ferreira, T. Santos, L. Ferreira, and L. Bernardino, Nanoparticle-mediated brain drug delivery: Overcoming blood-brain barrier to treat neurodegenerative diseases, J. Controlled Release **235**, 34 (2016).
[55] C. Yan, J. Gu, S. Yin, H. Wu, X. Lei, F. Geng, N. Zhang, and X. Wu, Design and preparation of naringenin loaded functional biomimetic nano-drug delivery system for Alzheimer's disease, J. Drug Target. **32**, 80 (2024).
[56] R. Yasuda and H. Murakoshi, The mechanisms underlying the spatial spreading of signaling activity, Curr. Opin. Neurobiol. **21**, 313 (2011).
[57] F. Santamaria, S. Wils, E. De Schutter, and G. J. Augustine, Anomalous diffusion in Purkinje cell dendrites caused by spines, Neuron **52**, 635 (2006).
[58] F. H. Kreten, B. A. Niemeyer, L. Santen, and R. Shaebani, Tracking the morphological evolution of neuronal dendrites by first-passage analysis, Biophys. J. **125**, 64 (2026).
[59] F. H. Kreten, L. Santen, and R. Shaebani, Dataset for "Transport-generated signals uncover geometric features of evolving branched structures", Zenodo (2026), doi: 10.5281/zenodo.18330000.
[60] R. Zwanzig, Diffusion past an entropy barrier, J. Phys. Chem. **96**, 3926 (1992).
[61] C. W. Gardiner, *Handbook of Stochastic Methods for Physics, Chemistry and the Natural Sciences*, *Springer Series in Synergetics*, 2nd ed. (Springer, Berlin, 1997), Vol. 13.
[62] N. Van Kampen, *Stochastic Processes in Physics and Chemistry* (Elsevier Science, The Netherlands, 2011).
[63] E. R. Weibel, *Morphometry of the Human Lung* (Springer, Berlin, 1963).
[64] T. F. Sherman, On connecting large vessels to small. The meaning of Murray's law, J. Gen. Physiol. **78**, 431 (1981).
[65] J. M. Newby and P. C. Bressloff, Quasi-steady state reduction of molecular motor-based models of directed intermittent search, Bull. Math. Biol. **72**, 1840 (2010).
[66] A. M. Berezhkovskii and L. Dagdug, Analytical treatment of biased diffusion in tubes with periodic dead ends, J. Chem. Phys. **134**, 124109 (2011).
[67] S. Verbanck and M. Paiva, Gas mixing in the airways and airspaces, Compr. Physiol. **1**, 809 (2011).
[68] B. Haefeli-Bleuer and E. R. Weibel, Morphometry of the human pulmonary acinus, Anat. Rec. **220**, 401 (1988).
[69] P.-R. Burgel, The role of small airways in obstructive airway diseases, Eur. Respir. Rev. **20**, 023 (2011).
[70] M. van den Berge, N. H. ten Hacken, J. Cohen, W. R. Douma, and D. S. Postma, Small airway disease in asthma and COPD: Clinical implications, Chest **139**, 412 (2011).
[71] A. B. Crawford, M. Makowska, M. Paiva, and L. A. Engel, Convection- and diffusion-dependent ventilation maldistribution in normal subjects, J. Appl. Physiol. **59**, 838 (1985).
[72] S. Verbanck, D. Schuermans, A. Van Muylem, M. Paiva, M. Noppen, and W. Vincken, Ventilation distribution during histamine provocation, J. Appl. Physiol. **83**, 1907 (1997).
[73] W. M. Gold and L. L. Koth, Chapter 25: Pulmonary function testing, in *Murray and Nadel's Textbook of Respiratory Medicine*, edited by V. C. Broaddus, R. J. Mason, J. D. Ernst, T. E. King, S. C. Lazarus, J. F. Murray, J. A. Nadel, A. S. Slutsky, and M. B. Gotway, 6th ed. (W.B. Saunders, Philadelphia, PA, 2016), p. 407.
[74] P. D. Robinson, *et al.*, Consensus statement for inert gas washout measurement using multiple- and single-breath tests, Eur. Respir. J. **41**, 507 (2013).
[75] E. R. Weibel, B. Sapoval, and M. Filoche, Design of peripheral airways for efficient gas exchange, Respir. Physiol. Neurobiol. **148**, 3 (2005).